Linear Stability Analysis of Wall-Bounded Flows Across Anisotropic Porous Media

Linear stability analysis of wall-bounded flows across anisotropic porous media

Thomas P. Hunter*
Delft University of Technology, Delft 2629HS, The Netherlands

Nguyen Anh Khoa Doan†
Imperial College, London SW7 2BX, United Kingdom

Francesco Avallone‡
Politecnico di Torino, Torino 10129, Italy

and
Daniele Ragni§
Delft University of Technology, Delft 2629HS, The Netherlands

A simplified model to study the physical mechanisms leading to tonal noise in noise-reducing trailing edges comprises communicating channels through a porous medium. The impact of material properties and flow conditions on the onset of the communication is investigated through a linear stability analysis based on a coupled Orr-Sommerfeld equation, modeling the porous medium using the Forchheimer-corrected Darcy law. The solution of the generalized eigenvalue problem results in the identification of three different instabilities: fluid, porous grazing, and communicating. The communication regime is the most unstable for thin porous media (t/δ < 3, t the thickness and δ the half-channel height) and at low bulk velocity Reynolds number (Re_b > 95). It is characterized by an increase in correlation and instantaneous flow between the channels. Moreover, the growth rate of the instability shows a dependence on the anisotropy of the porous medium properties, with wall-normal properties modulating the onset of communication. A velocity differential between the channels reduces the instantaneous flow through the porous medium and the correlation between the channels, explaining some of the communication reduction of porous trailing edges at lifting conditions. Design criteria of porous trailing edges are formulated to prevent the emergence of tonal noise at high permeabilities. The porous trailing edge should be: thin ($t/\delta < 2$), shorter than 6δ, and the permeabilities should be large enough ($Da > 6 \times 10^{-4}$ and $Fo > 4 \times 10^{-1}$, where Da and Fo are the traces of the linear and non-linear permeabilities respectively normalised with respect to the porous thickness).

*Doctoral Candidate, Aerodynamics Department-Faculty of Aerospace Engineering, `t.p.hunter@tudelft.nl`
†Associate Professor, Department of Aeronautics-Faculty of Engineering
‡Professor, Department of Mechanical and Aerospace Engineering
§Associate Professor, Wind Energy Department-Faculty of Aerospace Engineering

Nomenclature

α	=	perturbation wavenumber
$\mathbf{C}$	=	non-linear permeability tensor
δ	=	half-channel height
f	=	fluid activation function
ϕ	=	permeability anisotropy angle
$\mathbf{K}$	=	permeability tensor
λ	=	perturbation wavelength
L_i	=	domain dimension along the i-th direction
μ	=	dynamic viscosity
N	=	number of points
ν	=	kinematic viscosity
ω	=	perturbation growth rate
p	=	pressure
ψ	=	non-linear permeability anisotropy angle
ρ	=	density
Re_b	=	bulk Reynolds number
Re_τ	=	friction Reynolds number
s	=	solid activation function
t	=	porous medium thickness
θ_C	=	non-linear permeability off-diagonal angle
θ_K	=	linear permeability off-diagonal angle
$\mathbf{u}$	=	velocity vector
U	=	base flow
U_b	=	bulk velocity
ξ	=	velocity difference angle

I. Introduction

The reduction of turbulent boundary layer trailing edge noise, herein referred to as trailing edge noise, is of great interest to the wind energy sector [1]. Porous trailing edges mainly present the potential of being more effective in a wider range of operating conditions with respect to state-of-the-art noise mitigation solutions, such as serrations [2].

The noise reduction process relies on both sides of the airfoil communicating [3], referred to as the pressure release mechanism [4]. The pressure release mechanism is related to the interaction between the unsteady pressure fluctuations across the airfoil sides [5]. While the communication is a necessary condition to the noise reduction, to the authors' knowledge, the rigorous characterisation of communication has not been established.

A series of assumptions can be made in order to characterize the communication specifically. First, the geometry of the trailing edge can be simplified to that of a porous flat plate, similarly to bio-inspired analytical approaches [6]. Second, the problem of turbulent boundary layers interacting with porous media can be cut down to simpler wall-bounded flows. For instance, the analysis of turbulent channel flows over porous media has been simplified to that of channel flows over porous media [7], and acoustic liners [8]. This latter simplification greatly reduces computational cost, enabling the solution of flows over both pore-resolved [9] and modeled porous media [10]. In experimental studies of porous trailing edges, spurious tonal noise and altered aeroacoustic performance were observed with changes in material properties and flow conditions. Namely, at high permeabilities, when noise reduction was expected to be largest, a tonal signature was documented for certain geometries [11, 12], and large losses in aerodynamic performance were noted [3, 13]. Additionally, the noise reduction potential decreased at lifting conditions [14].

The tonal noise source was identified in the pore-resolved results of the communicating channel flows [15]. The latter study identified a fully developed communicating regime dominated by strong spanwise coherent turbulent structures, similar to a shear instability mode with a turbulent coherence length based Strouhal number of $St_L = 0.22$. While qualitatively similar to the shear instability described in literature for grazing flows over porous media of high permeability [7], the communicating regime was documented to be independent of the porous grazing flow regime [16, 17]. Additionally, the spanwise coherent structures were associated with a large drag increase. The flow modifications did not appear to be related to geometrical parameters or material properties usually related to grazing flows over porous media [8]. Given the significance of communicating flow through porous media, the communicating regime, and the noted instability, building an understanding of dependency on porous medium parameters is of importance to diagnose undesired behaviours in porous trailing edges.

Porous medium properties have been documented to greatly influence the aeroacoustic performance of porous trailing edges. The linear permeability was identified as the primary variable for the noise reduction potential [11]. The Forchheimer correction, or non-linear permeability, was also observed to play an important role both in the noise prediction [18], but also in the regulation of the noise signature [12]. In the latter study, with large values of permeability, a tonal noise signature was noted, and the modification of the non-linear permeability enabled a reduction of the shedding-induced tone. The shedding was a direct result of the anti-correlation of the pressure fluctuations on the two sides of the porous medium, resulting in an instantaneous pressure differential across the medium and the flow through the medium.

Previous work has studied the extent to which the porous medium promotes the breakdown of flow structures. Approaches modeling the porous medium with the Darcy law found the rollers to be related to the depth and permeability of the porous medium with a dependence on the direction of the porous properties [19]. Similar instabilities were observed when modeling the porous medium with the Forchheimer correction in sea-grass beds [20], or the Brinkman equation for porous walled channel flows [16]. Using both terms in the Forchheimer-corrected Darcy law, similar instabilities at the surface of the porous medium were observed to be the most unstable modes [21]. While the linear stability of communicating wall-bounded flows has not been studied in and of itself, in the process of studying the transition of porous-walled channels by vertically layering channels and porous media [22, 23], it was observed that the critical Reynolds number decreased with the porous medium thickness. Based on these findings, it is hypothesized that the latter instability is a communication-induced instability, and its relationship to material and flow properties warrants further investigation. Finally, it is hypothesized that the impact of communication and the onset of the flow modifications are primarily hydrodynamic and can therefore be captured with a laminar linear stability analysis. It is noted that resolvent turbulent stability analyses have been conducted for grazing flows over flow-modifying features such as riblets [24], transpiring walls [25], and porous substrates [26, 27], for instance.

The goal of this study is to investigate the impact of porous medium design parameters and their relationship to flow conditions, on the onset of communication-induced flow modifications using linear stability analysis. Applying the aforementioned simplifications to communicating turbulent boundary layers results in a multi-layered channel flow that has been used previously [15, 17]. The resulting setup resembles Refs. [22, 23], although these result from geotechnical and industrial settings. As a consequence, using a multi-layered channel flow eliminates the effects of variations in thickness and streamwise pressure gradient encountered in porous trailing edges. Additionally, the setup allows for the control of flow differences in both interacting wall-bounded flows and for reducing the computational cost of pore-resolved turbulent boundary layer simulations. The linear stability analysis is achieved by deriving a fully coupled Orr-Sommerfeld system of equations that enables the investigation of the effect of porous media permeability, thickness, and flow conditions on the linear stability of communicating flows. From these results, design criteria of porous trailing edges are obtained to prevent the emergence of a tonal acoustic signature, and associated loss in aerodynamic performance, from the investigation of the underlying mechanism and not simply observation. The main contribution of this work is the systematic study of the linear stability of communicating channel flows over a wide range of thin and highly anisotropic porous media, modeled with full permeability tensors.

We present the methodology in section II. Specifically, in subsection II.C we detail the derivation of the base flow solution, and in subsection II.D the derivation of the modified Orr-Sommerfeld equation of the setup. We show the results of the analysis in section III. We document the comparison to the results of the pore-resolved simulations from [15]. We investigate the sensitivity of the system to material parameters and flow conditions in section IV, and summarize the main results of the study in section V.

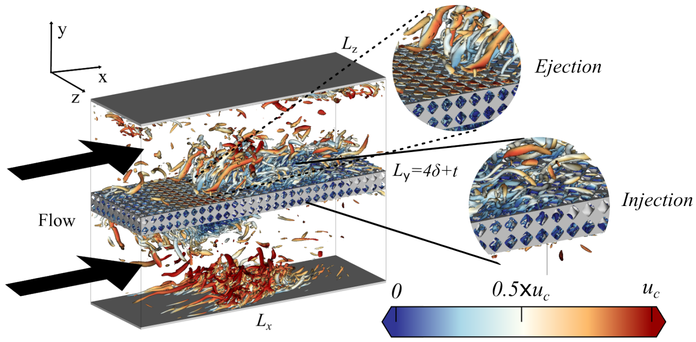

Fig. 1 Isosurfaces of constant $\lambda_2 = -2 \times 10^7$ s^{-2}, coloured by the streamwise velocity for the C-TCF. Adapted with permission from Hunter et al. [15]. Copyright 2025 Hunter.

II. Methodology

For the purpose of this study, we choose to investigate the onset of the communicating regime of wall-bounded flows separated by a thin porous medium. Building on previous studies, where the communication between turbulent boundary layers was found to be a necessary condition for noise reduction (both experimentally [4] and numerically [28]), we continue to explore the effect of communication alone between wall-bounded flows to understand its driving mechanisms.

A. Computational domain and assumptions

Consistent with previous studies [15, 17], we simplify the analysis of the onset of communication in porous trailing edges by eliminating the impact of streamwise pressure gradient changes, streamwise spatial boundary layer development, trailing edge geometry, and porous medium geometry by considering a flat plate of modeled porous medium separating two channel flows. While in appearance similar to the numerical setup of Hunter et al. [15] illustrated in Figure 1 where the dimensions of the domain were $L_x \times L_y \times L_z = 6\delta \times (4\delta + t) \times 2\delta$, we use the strong spanwise correlation of these prior results to make the assumptions that the analysis can be simplified to a two-dimensional computational domain, as shown in Figure 2 where the streamwise length is a free parameter. We also choose to use closed channels on the top and bottom, in opposition to open channels [29] or turbulent boundary layers [30], since the former does not allow for the unimpeded growth of instabilities spanning more than δ in the wall-normal extent, and the latter has no streamwise homogeneous or self-similar solution.

The two channels are driven by a constant forcing $F_{forcing}$. The forcing is mathematically equivalent to a pressure gradient and enables a statistically stationary solution to the channel flow setup, without a physical pressure gradient. Due to the presence of two channels, independent forcing can be set in the top and bottom channels using the following definition:

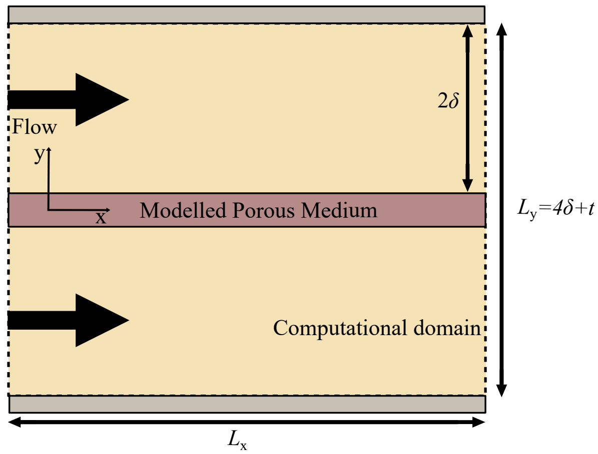

Fig. 2 Computational domain of the linear stability analysis.

$$F_{forcing} = \begin{cases} -F_{top},\ y >= 0 \\ \\ -F_{bottom},\ y < 0 \end{cases} \tag{1}$$

Based on this definition of the forcing, we can define the velocity differential angle $\xi = \text{atan}\left(\frac{F_{bottom}}{F_{top}}\right)$, which reflects the velocity differential obtained by the differential forcing across the channels.

In turn, with the proposed analysis that we detail in the following sections, we can go further than the existing literature by exploring the temporal development of the communication and relating this onset to porous medium properties and flow conditions.

B. Porous medium modeling

We model the relationship between the pressure drop and flow rate through the porous medium using the Darcy-Forchheimer equation. This set of governing equations assumes an incompressible, statistically stationary, and homogeneous flow through porous media for moderate to high pore diameter based Reynolds number ($10 < Re_d < 10^3$) [31]. For grazing flows over acoustic liners [32], and pore-resolved simulations of communicating channel flows [15], this is the dominating flow regime. The Darcy-Forchheimer has been extensively used in literature for the modeling of porous media in Joseph et al. [33], Wang et al. [34], Aghaei-Jouybari et al. [35]. Additionally, this modeling approach has been used in previous modal and non-modal stability analyses of grazing flows over porous media [20, 36, 37], further extending the model to unsteady analysis. Finally, both linear and non-linear permeabilities were shown to be important to the noise reduction [12, 18]. Specifically, we use the dimensional formulation:

$$F_{porous} = -\nabla p = \mu \mathbf{K}^{-1} \cdot \mathbf{u} + \rho \mathbf{C}^{-1} \cdot \mathbf{u}|\mathbf{u}|. \tag{2}$$

The equation reads that the gradient of the pressure p is related to the through velocity $\mathbf{u}$ via the second-order (linear) permeability tensor $\mathbf{K}$ and the non-linear permeability tensor $\mathbf{C}$, as well as the dynamic viscosity μ and the density ρ. We denote K_{ij} the component of the tensor with entry (i, j). The diagonal terms are therefore K_{11} and K_{22} and correspond to the wall-normal and streamwise directions, respectively. This formulation allows us to describe anisotropic porous media used for trailing edge noise abatement, such as perforations [38], or combs [39]. Moreover, the off-diagonal terms of the permeability tensors relate to the steering effect that certain regular porous media offer, and tend to be negligible for metal foams and stochastic porous media [35].

With the addition of the continuity equation, the forcing driving the channels, and the drag imparted by the porous medium, we obtain the following system of equations:

$$\begin{cases} \nabla \cdot \mathbf{u} & = 0 \\ \frac{\partial \mathbf{u}}{\partial t} + (\mathbf{u} \cdot \nabla)\mathbf{u} & = -\nabla \frac{p}{\rho} + \nu \nabla^2 \mathbf{u} \\ & \quad + F_{forcing} - F_{porous}, \end{cases}$$

where ν is the kinematic viscosity.

Combining this expression with the definition for the forcing from Equation 1, and for the porous drag in Equation 2, results in Equation 3.

$$\begin{cases} \nabla \cdot \mathbf{u} & = 0 \\ \frac{\partial \mathbf{u}}{\partial t} + (\mathbf{u} \cdot \nabla)\mathbf{u} & = -\nabla \frac{p}{\rho} + \nu \nabla^2 \mathbf{u} \\ & \quad + f(y) F_{forcing} - s(y) \left(\mu \mathbf{K}^{-1} \cdot \mathbf{u} + \rho \mathbf{C}^{-1} \cdot \mathbf{u}|\mathbf{u}| \right). \end{cases} \tag{3}$$

In this equation, we define the activation functions $f(y) = 1$ (for fluid) in the parts of the domain where the forcing is applied (here, it is outside of the porous medium) and zero elsewhere, and the complementary function $s(y) = 1$ (for solid) in the porous medium.

Flow parameters of interest As part of the study of the sensitivity of the interacting channels through porous media, we identify key parameters of interest, namely: the thickness ratio t/δ, the bulk Reynolds number Re_b (obtained from the measured bulk velocity defined below), and the velocity differential angle $\xi = \text{atan}\left(\frac{F_{bottom}}{F_{top}}\right)$.

Material parameters of interest We also identify porous media properties of interest stemming from the linear permeability tensor $\mathbf{K}$, and the non-linear permeability tensor $\mathbf{C}$. We define the additional parameters: the Darcy number $Da = \text{Tr}(\mathbf{K})/t^2$, the Forchheimer number $Fo = \text{Tr}(\mathbf{C})/t$, the preferential angles $\phi = \text{atan}(\frac{K_{22}}{K_{11}})$ and $\psi = \text{atan}(\frac{C_{22}}{C_{11}})$, their diagonal dominance angles $\theta_K = \text{atan}(\frac{2K_{12}}{\text{Tr}(\mathbf{K})})$ and $\theta_C = \text{atan}(\frac{2C_{12}}{\text{Tr}(\mathbf{C})})$, driving the steering effect [35], and the porous

Reynolds number $Re_{K/C} = \frac{u_b \mathrm{Tr}(\mathbf{K})/\mathrm{Tr}(\mathbf{C})}{\nu}$.

C. Base flow

We calculate the fully developed one-dimensional stationary solution $\mathbf{U} = [U(y), 0]^T$, $\forall\, y \in [-2\delta - t/2,\, 2\delta + t/2]$ by solving the momentum balance of Equation 3. We obtain:

$$f(y)F_{forcing} + \nu U''(y) - s(y)\left(\nu\frac{K_{22}}{\det(\mathbf{K})}U + \frac{C_{22}}{\det(\mathbf{C})}U|U|\right) = 0, \tag{4}$$

where $\forall\, |y| < t/2,\ s(y) = 1, \forall\, |y| > t/2,\ f(y) = 1$, and both are zero otherwise. We omit the activation functions in the rest of the derivations.

We solve this equation iteratively for U and the required forcing to obtain an objective Reynolds number $Re_b = \frac{\rho U_b \delta}{\mu}$, using a fourth-order central finite-difference scheme. The definition of the bulk velocity reads:

$$U_b = \frac{1}{4\delta + t}\int_{-2\delta-t/2}^{2\delta+t/2} f(y)U dy \tag{5}$$

This equation is evaluated using the trapezoidal method.

We note that the base flow depends only on the streamwise material properties of the porous medium. This indicates that the variation of the wall-normal properties does not influence the base flow, while the streamwise properties will likely induce a larger modification of the response of the LSA due to changes in both the base flow and perturbations. We note that the wall-normal properties do not appear in this work since we assume the wall-normal velocity in the base flow to be zero, which would not be the case for all wall-bounded flows.

We show a typical base flow obtained using the parameters from Table 1 in Figure 3. These parameters are taken to provide comparable flow conditions and material properties to the existing literature where the noise reduction is maximal and tonal noise sometimes appears [4, 40, 41], and are identical to the ones where the shedding-like instability was documented [15, 17]. We can see that the base flow obtained is made up of two Poiseuille flow solutions in the channels with a slip velocity at the porous medium boundary. In the channels, the profile is parabolic, and it is more complex in the porous medium due to the additional drag.

We choose to match the bulk Reynolds number when comparing to the turbulent simulations, instead of the forcing magnitude. This is based on the observation that matching pressure gradients for higher Reynolds number cases leads to laminar bulk velocities being extremely large and outside of the envelope where LSA could be applicable.

Table 1 Reference material and flow properties from Ref. [15].

Property	Value
$\mathbf{K}$ $[m^2]$	$\begin{bmatrix} 3.917 & 0 \\ 0 & 4.703 \end{bmatrix} \times 10^{-8}$
$\mathbf{C}$ $[m]$	$\begin{bmatrix} 1.108 & 0 \\ 0 & 3.520 \end{bmatrix} \times 10^{-3}$
t/δ	0.04
Re_b	4.5×10^3
ρ $[kg/m^3]$	1.225
μ $[kg/m/s]$	1.789×10^{-5}
δ $[m]$	1×10^{-2}

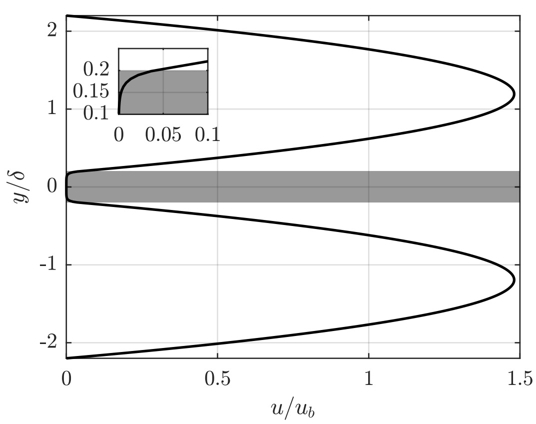

Fig. 3 Base flow for the reference setup, using the parameters of Table 1.

D. Modified Orr-Sommerfeld equation

We linearise Equation 3 using the expansion $\mathbf{u}(\mathbf{x},t) = \mathbf{U}(\mathbf{x}) + \mathbf{u}'(\mathbf{x},t)$, around a steady base flow $\mathbf{U} = [U(y), 0]^T$:

$$\begin{cases} \nabla \cdot \mathbf{u}' & = 0 \\ \partial_t \mathbf{u}' + (\mathbf{U} \cdot \nabla)\mathbf{u}' + (\mathbf{u}' \cdot \nabla)\mathbf{U} & = -\frac{1}{\rho}\nabla p' + \nu \nabla^2 \mathbf{u}' \\ & \quad -\nu \mathbf{K}^{-1} \cdot \mathbf{u}' - \mathbf{C}^{-1} \cdot \mathbf{u}'|\mathbf{U}|. \end{cases} \tag{6}$$

We expand and simplify this system of equations in the homogeneous directions and obtain:

$$\begin{cases} \partial_x u' + \partial_y v' & = 0 \\ \partial_t u' + U\partial_x u' + v'\partial_y U & = -\partial_x p' + \nu\partial_{xx} u' + \nu \partial_{yy} u' \\ & \quad -\nu \frac{K_{22}}{\det(\mathbf{K})} u' - \frac{C_{22}}{\det(\mathbf{C})} u'U \\ & \quad +\nu \frac{K_{12}}{\det(\mathbf{K})} v' + \frac{C_{12}}{\det(\mathbf{C})} v'U \\ \partial_t v' + U\partial_x v' & = -\partial_y p' + \nu\partial_{xx} v' + \nu\partial_{yy} v' \\ & \quad -\nu \frac{K_{11}}{\det(\mathbf{K})} v' - \frac{C_{11}}{\det(\mathbf{C})} v'U \\ & \quad +\nu \frac{K_{12}}{\det(\mathbf{K})} u' + \frac{C_{12}}{\det(\mathbf{C})} u'U. \end{cases} \tag{7}$$

We then substitute the perturbations $\mathbf{u}' = [u', v']^T$ assuming wave-like solutions of the form $\mathbf{u}'(x,y,t) = (u'(y), v'(y))^T e^{i(\alpha x - \omega t)}$. The pressure is eliminated by coupling the two momentum equations, and we use continuity to express u' in terms of v'. We obtain the following coupled Orr-Sommerfeld equations:

$$\begin{cases} -i\alpha U(D^2 - k^2)v' + i\alpha U''v' + \nu(D^2 - k^2)^2 v' \\ -(\nu \frac{K_{22}}{\det(\mathbf{K})} + \frac{C_{22}}{\det(\mathbf{C})} U) D^2 v' - \frac{C_{22}}{\det(\mathbf{C})} U' D v' = -i\omega(D^2 - k^2)v' \\ +k^2(\nu \frac{K_{11}}{\det(\mathbf{K})} + \frac{C_{11}}{\det(\mathbf{C})} U)v' \\ -i\alpha(2\nu \frac{K_{12}}{\det(\mathbf{K})} + 2\frac{C_{12}}{\det(\mathbf{C})} U + \frac{C_{12}}{\det(\mathbf{C})} U')Dv'. \end{cases} \tag{8}$$

We perform the linear stability analysis by solving the generalized eigenvalue problem of the form $\mathbf{A}v' = \omega \mathbf{B}v'$, for a chosen wavenumbers α and with boundary conditions $v'(\pm(2\delta + t/2)) = \frac{dv'}{dy}|_{\pm(2\delta+t/2)} = 0$. The growth rate ω corresponds to the eigenvalues and the perturbation v' that of the eigenvectors of the problem. The wavelength of the perturbations is then $\lambda = 2\pi/\alpha$. The derivatives of the base flow are computed using a second-order finite-difference scheme. Based on the present results, we have not found the need to incorporate smoothing, domain separation, or matching conditions at the interface. We solve the problem numerically using a fourth-order central finite-difference scheme on a uniform grid and the sparse eigenvalue solver found in MATLAB, solving for the 20 eigenvalues with the largest imaginary component. For each wavenumber, we identify unstable modes as the ones having $\mathrm{Im}(\omega) > 0$.

In this work, we will characterize the dominating instability (the largest growth rate $\max(\mathrm{Im}(\omega) > 0)$ for each perturbation wavelength λ), and relate it to porous media properties. The properties of interest are: the relative thickness t/δ, the linear permeability tensor $\mathbf{K}$, and the non-linear permeability tensor $\mathbf{C}$. Different flow conditions are considered by varying the bulk Reynolds number Re_b and the velocity differential angle ξ.

III. Linear stability of communicating channels

In the pore-resolved simulations of communicating turbulent channel flows across porous media, a shedding-like instability, which is characterised by strong spanwise coherent turbulent structures, were documented [15]. The anti-symmetry of the spanwise structures between the two channels led to instantaneous mass flow through the porous medium ($v^+_{through} \approx 1$, where $v^+_{through}$ is the viscous scaled maximum instantaneous flow through). This flow through was driven by an instantaneous pressure differential between the channels ($R(\Delta p_{predicted}, \Delta p_{measured} \approx 0.82)$, where R is the cross-correlation between predicted and measured pressure differential based on the flow through the porous medium).

With the present study, we will compare these results with the ones obtained with the LSA based on the same material parameters. Since the LSA does not incorporate parameters related to the porous medium geometry (such as the pore diameter), we seek to identify the parameters relevant to the hydrodynamic instability of the aforementioned communication-induced shedding.

A. Neutral curve

The first linear stability characteristic of the setup is its neutral curve. This corresponds to the curve where $\mathrm{Im}(\omega) = 0$ as a function of the perturbation wavelength and the Reynolds number. This curve, and the growth rate at other combinations of wavelength and Reynolds number, inform us on the critical points of the interacting channel flows through porous media, such as the critical Reynolds number and the critical wavelength. We vary the spatial wavelength of the perturbations λ/δ and the bulk Reynolds number Re_b in order to estimate the position of the neutral curve of the setup. We use the reference material parameters as documented in Table 1 for this figure.

We show the neutral curve and the growth rate of the most unstable mode as a function of the forcing and the wavelength of the mode in Figure 4. In Figure 4 (a), we can see that there exists a critical bulk Reynolds number of 95, below which the system is linearly stable. This is much lower than the critical bulk Reynolds number for a Poiseuille flow $Re_b = 3.85 \times 10^3$ documented in Orszag [42]. This latter critical mode for Poiseuille flow is here called the fluid mode.

We seek to characterize the most unstable mode of the communicating channels. Therefore, we plot the eigenvalue trajectory of the dominating unstable modes as a function of the perturbation wavelength, as shown in Figure 4 (b).

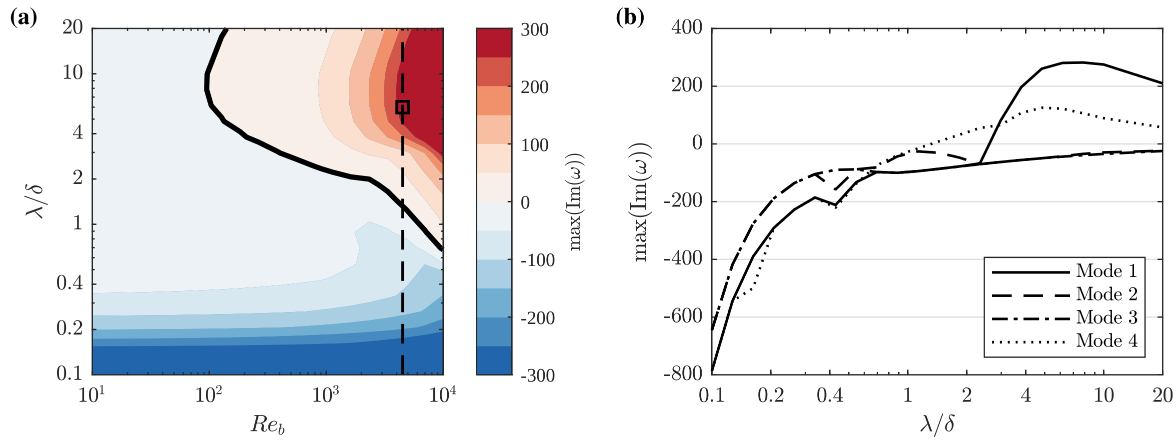

Fig. 4 Growth rate as a function of wavelength (a) and bulk Reynolds number for the most unstable mode, and (b) at $Re_b = 4.5 \times 10^3$ (dashed line in (a)) for the four fastest-growing perturbations.

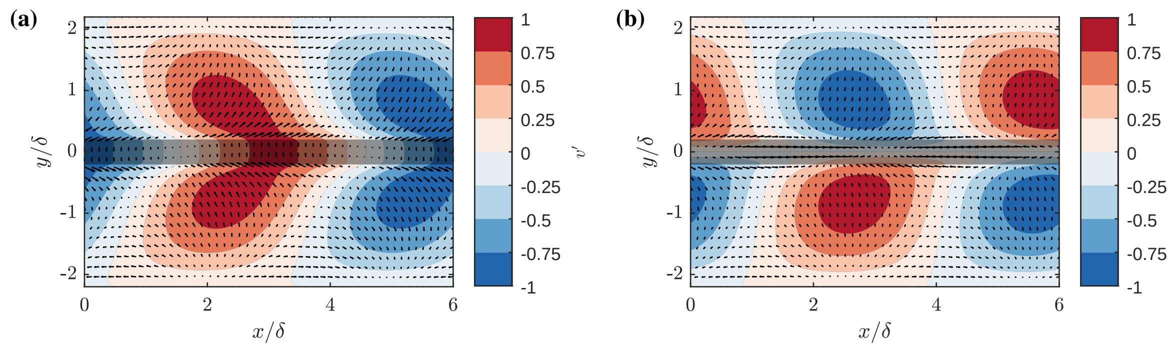

Fig. 5 Contours of the normalised wall-normal velocity eigenfunction, with the arrows indicating the local flow direction, for $\lambda/\delta = 6$, $Re_b = 4.5\times10^3$, with (a) Mode 1, and (b) Mode 4 of Figure 4 (b).

We observe that for the range of velocities and wavenumbers considered, the system is linearly stable for wavelengths $\lambda/\delta > 1$. The dominating instability corresponds to Mode 1, which we show in Figure 5 (a). Due to the flow going through the porous medium from one channel to the other, this is likened to the communication mode described in Karmakar et al. [23]. This mode is distinct from the grazing flow instability documented in Singh et al. [20] where the largest magnitude of the perturbation is above the interface with the porous medium, while in this study it is situated at the interface.

Existing work showed a shedding-like behaviour of wavelength $\lambda/\delta = 5.4$, double the coherence length [15, 17]. We find that the system presents a bifurcation between linearly stable and unstable around a wavelength of $\lambda/\delta = 1$ in the LSA, with the most unstable mode at a wavelength of $\lambda/\delta = 6$. This corresponds to a comparable wavelength of the shear instability in the pore resolved simulation, where from the spatio-temporal correlation map, a wavelength of $\lambda/\delta = 5.4$ was found.

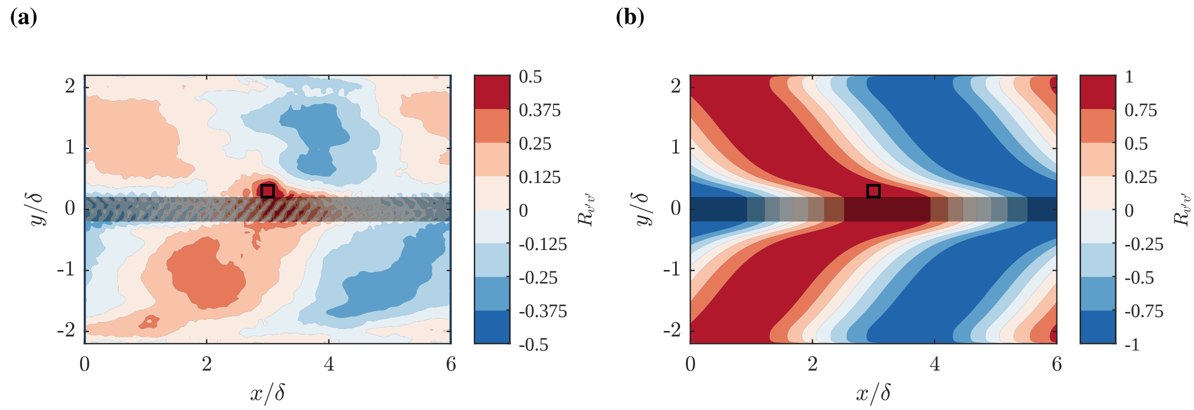

Fig. 6 Cross-correlation of the wall-normal velocity fluctuation about the square, $(x/\delta,\ y/\delta) = (3,\ 0.3)$, in a $x - y$ plane for (a) the pore-resolved simulation [15] and (b) the LSA.

B. Communication mode definition

We seek to formalize the definition of the communication to quantify the similarity of the results of the LSA and those of the pore-resolved simulations.

We choose to define the cross-correlation of the wall-normal velocity as a metric to quantify communication. In order to verify that this method for the quantification of communication is valid, we compare the cross-correlation maps of the wall-normal velocity obtained by the LSA and the pore-resolved simulations in Figure 6.

In this figure, we show the cross-correlation of the wall-normal velocity fluctuation between a reference point in the center of the visualisation and the rest of the field. In the aforementioned study [15], the wall-normal component is heavily modified, and due to the instantaneous flow through the porous medium, there is a significant correlation between the two channels. We find that both the LSA and the pore-resolved simulation converge to a similar correlation map. We attribute the differences to the pore-resolved simulation being noisier due to the turbulent nature of the simulation. However, the same mode dominates in both the laminar LSA and the turbulent pore-resolved simulation, giving us confidence in the results of the present study.

Since the sole presence of a correlation does not indicate whether or not there is momentum or mass transfer between the channels, we also compute the mass flow rate about the porous medium at different streamwise locations. We choose to cut the porous medium into volumes of $t \times 0.2\delta$ in the wall-normal and streamwise directions, respectively. For each volume, we compare the values of the mass flow rate going through the left, right, bottom, and top boundaries. We show the results in Figure 7 (a). There is an alternating mass flow between the top and bottom channels induced by the most unstable mode. The net mass flow in each of the volumes remains zero, highlighting that the flow through the porous medium is solely in the vertical direction. We can therefore expect that the communication instability is related to the wall-normal permeabilities of the porous medium.

We can therefore determine if there is communication using the instantaneous mass flow through the porous medium

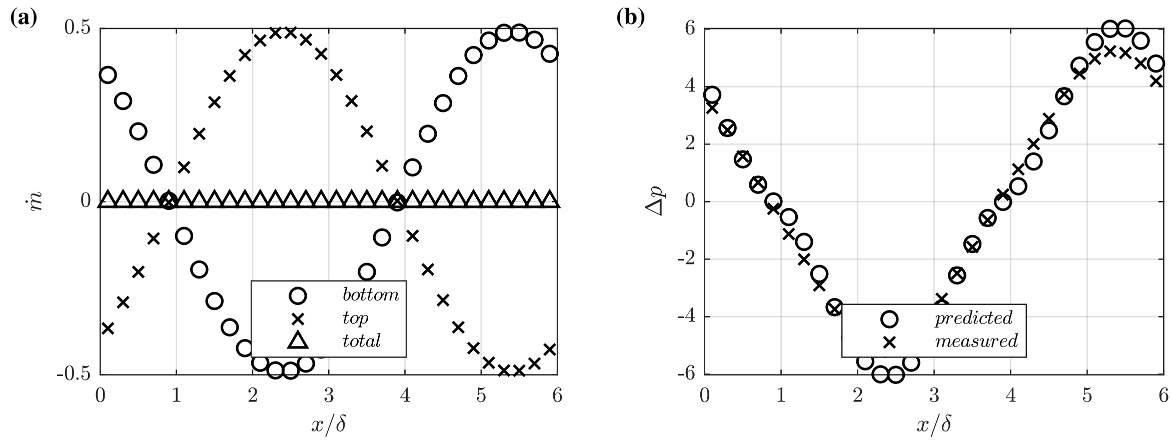

Fig. 7 (a) Mass flow rate and (b) predicted and measured pressure differential across the porous medium for $\lambda/\delta = 6$, $Re_b = 4.5 \times 10^3$, and the porous properties of Table 1.

and quantify the communication between wall-bounded flows using the correlation of the velocity fields.

We compute the pressure field from the velocity field shown in Figure 5 (a). Comparing the pressure difference between the top and bottom boundaries of the aforementioned volumes to the one predicted with the mass flow going from the top to the bottom channel in Figure 7 (b), we find that the Forchheimer-corrected Darcy law (in the wall-normal direction) fully captures the alternating upwards and downwards flow. This confirms that despite the base flow being modified by the streamwise material properties, the wall-normal porous properties modulate the strength of the communication mode, here the fastest growing perturbation.

Using these results, we determine a design criterion for a flat porous trailing edge to prevent the emergence of tonal noise resulting from spanwise coherent structures. The various modes have a shape $\mathbf{u'}(y)e^{i\alpha x}$ and a growth $e^{-i\omega t}$. We can assume that a given perturbation induced by the communication mode becomes significant when there is no longer a scale separation between the velocity through the porous medium and the bulk velocity ($v_{through}/U_b > 10\%$). By computing the through velocity $v_{through} = (v'_{top\,interface} + v'_{bottom\,interface})/2$, we can therefore find the associated growth time T before which the mode becomes significant. Using the Taylor hypothesis, we can make the argument that each mode is convected at a velocity $c = \mathrm{Re}(\omega/\alpha)$ over this advection time T. Considering the most critically amplified perturbation where the criterion $L_{porous} < c/T$ is smallest, we find that the velocity through the porous medium becomes significant after a porous trailing edge extension length of 6.7δ, corresponding to the fastest-growing perturbation at $\lambda/\delta = 6$. Therefore, we show that the communication-induced flow modifications occur rapidly and this new understanding thus limits the porous extent. We note that the convective velocity c varies with each perturbation, and its role in the eventual emergence of spanwise coherent structures in porous trailing edge extensions warrants further analysis that falls beyond the scope of the present work.

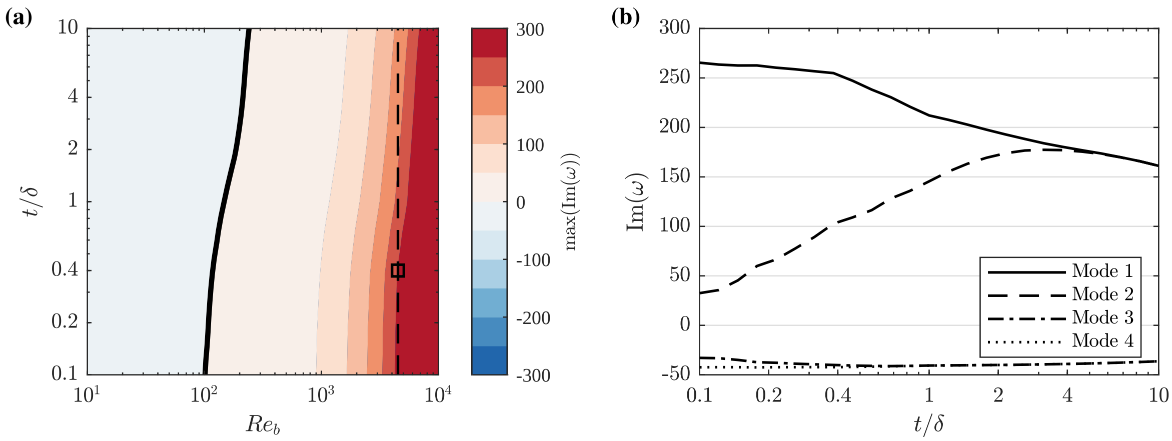

Fig. 8 Growth rate for $\lambda/\delta = 6$ as a function of relative thickness (a) and bulk Reynolds number, and (b) at $Re_b = 4.5 \times 10^3$ (dashed line in (a)) for the four fastest-growing perturbations.

IV. Communication modulation

We seek to further identify the driving parameters of the dominating instabilities. In particular, for the design of porous trailing edges, it would be beneficial to identify the design parameters affecting the communication whose growth is lower since this would prevent the emergence of noise associated with the shedding [12].

A. Porous medium thickness

We change the thickness of the porous medium to range $t/\delta \in [0.1,\ 10]$. We compute the most unstable modes as a function of thickness and forcing, forming the neutral curve in Figure 8 (a). We note that the properties **K** and **C** in the wall-normal direction (K_{11} and C_{11} respectively) become functions of the thickness ($K_{11}(t)$ and $C_{11}(t)$), where the value of the permeabilities vary following a log-law in the range $t/\delta \in$[0.4, 2] [43] between the values in Table 1 (e.g. for the permeability $K_{11}(0.4) = K_{11,table}$ and $K_{11}(2) = K_{22,table}$).

The growth of the leading unstable mode is mainly dependent on the Reynolds number. However, we can observe that instability characteristics vary with thickness, in particular around a critical thickness of $t = \delta$. As previously observed in another pore-resolved study of porous trailing edges [41], communication dominates for thicknesses and pore diameters of the same order as the boundary layer thickness. We show in the neutral curve that thinner porous media are more unstable at a given velocity.

Looking at the growth rate of the most unstable modes as a function of the thickness in Figure 8 (b), we see that over a thickness of 3δ, the dominating instability changes as two modes coalesce. As the thickness increases, the communication mode is no longer dominating, and a new mode where two instabilities dominate appears, which we call the porous grazing mode.

For completeness, we also investigate the linear stability of the varying thicknesses. We show the results in Figure 9. The most unstable mode that occurs across all thicknesses is the one corresponding to $\lambda/\delta = 6$. However, we also note

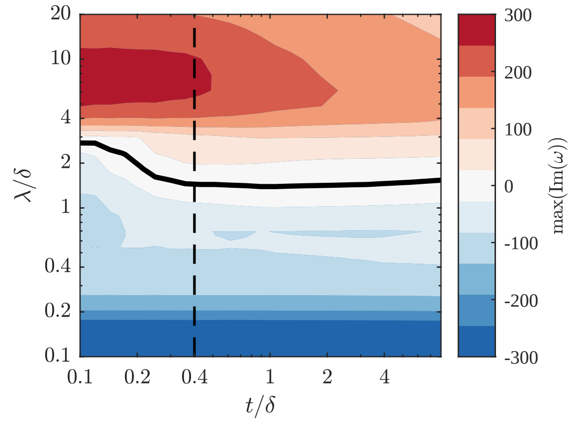

Fig. 9 Growth rate as a function of perturbation wavelength and relative thickness for Re_b = 4.5×10^3. The dashed line indicates the relative thickness of the reference setup.

that the communication mode is mainly present for larger perturbation wavelengths when the porous medium is very thin, $t/\delta < 0.2$. We can conclude that the communication mode is therefore the most unstable mode for thin porous media, and for large wavelengths.

We present, in Figure 10, the shape of the most unstable mode for thickness ratios of $t/\delta = 1$ and $t/\delta = 4$, at the same velocity. We observe a key difference with the perturbation magnitude being larger in the fluid for the thicker case, and in the porous medium for the thinner case (Figure 10 (a)). This key difference is responsible for the presence of the unstable communication mode. With increasing thickness, the velocity in the porous medium approaches zero. The velocity in both channels also becomes independent from one another as two modes dominate equally that have a phase angle in x of $\pi/2$ and are both coherent for Mode 1 (Figure 10 (b)) and out-of-phase for Mode 2 (Figure 10 (c)).

B. Velocity differential

We investigate the impact of the flow conditions on the linear stability of the communicating channels by varying the forcing and, as a result, the velocity in each channel. We liken this to porous trailing edges of a lifting airfoil [14, 44], where a velocity gradient is present across the trailing edge, and the wall-normal velocity is negligible at the airfoil-to-porous medium transition, or if the porous trailing edge is unloaded. For this purpose, we define a forcing preference direction $\xi = \text{atan}\left(\frac{F_{bottom}}{F_{top}}\right)$ and iteratively solve for a bulk velocity Re_b. An example base flow for a bulk Reynolds number of 4.5×10^3 and a forcing direction $\xi = 15°$ is given in Figure 11. For a fixed perturbation length $\lambda/\delta = 6$, we obtain a map of the growth rate of the most unstable mode as a function of both these parameters, as shown in Figure 12 (a). We note the symmetry about $\xi = 45°$ due to the symmetry of the setup, being representative of the absence of velocity differential.

From Figure 12 (a), we note that the velocity differential does not greatly modify the linear stability of the system. The stability map shows a strong dependence on the Reynolds number. We plot the trajectory of the eigenvalues of the

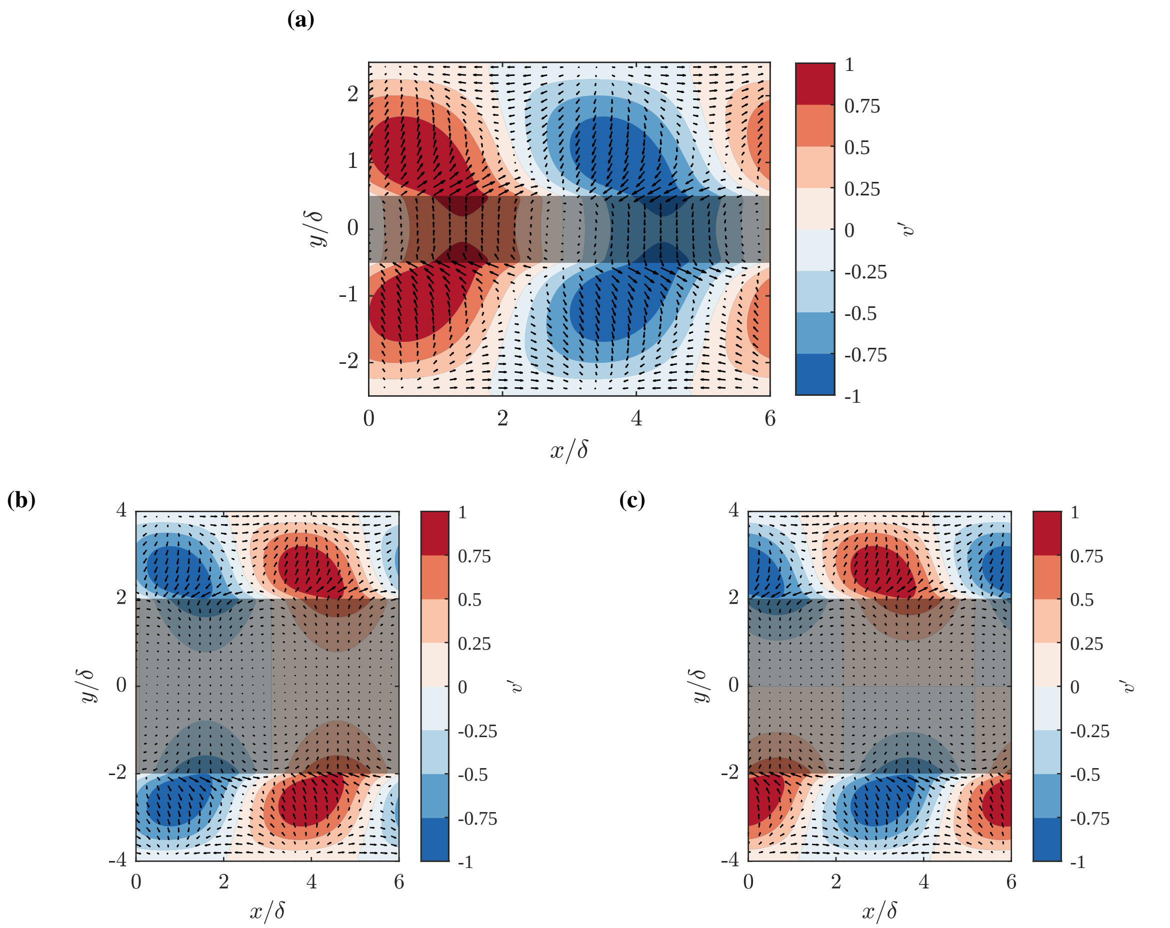

Fig. 10 Normalised wall-normal velocity eigenfunctions (arrows indicate flow direction), for the most unstable modes at (a) $t/\delta = 1$, and (b) the first and (c) second modes at $t/\delta = 4$.

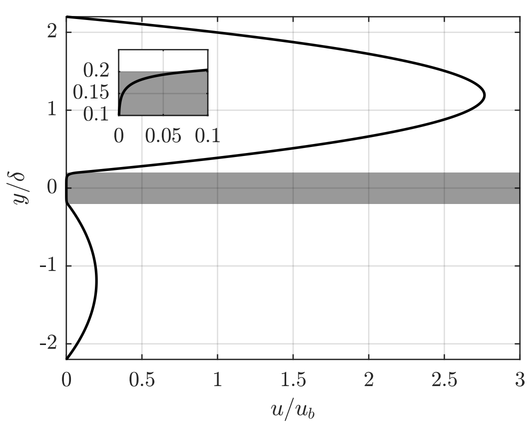

Fig. 11 Base flow at a fixed $Re_b = 4.5 \times 10^3$, pressure angle of $\xi = 15°$

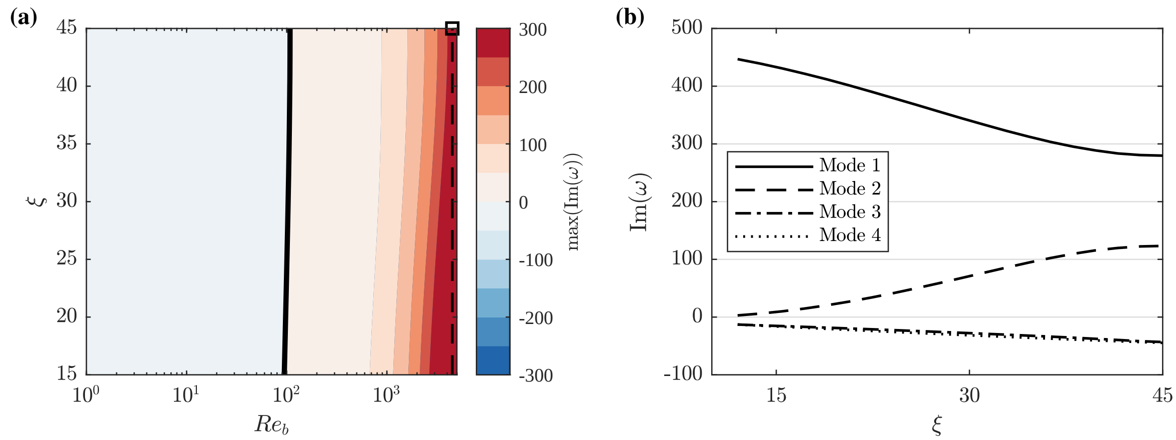

Fig. 12 Growth rate at $\lambda/\delta = 6$ as a function of the velocity differential (a) and bulk Reynolds number, and (b) at $Re_b = 4.5 \times 10^3$ (dashed line in (a)) for the four fastest-growing perturbations.

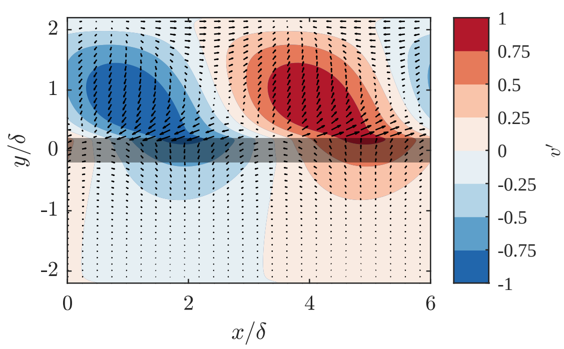

Fig. 13 Normalised wall-normal velocity, with the arrows indicating the local flow direction, for the most unstable mode shape at a pressure angle of $\xi = 15°$, $\lambda/\delta = 6$ and $Re_b = 4.5 \times 10^3$.

most unstable modes as a function of the velocity differential in Figure 12 (b). We observe that the instability grows with the velocity differential, with a marked increase occurring beyond $\xi > 40°$. This corresponds to a forcing ratio of ≈ 0.84 between the top and bottom channels. We hypothesize a change in the shape of the fastest growing perturbation beyond this forcing ratio.

We show the dominating instability in Figure 13. This linearly unstable mode shows an entrainment of the slower channel and the instability primarily growing in the faster channel through the porous medium. Considering the top channel, we see that the instability resembles the porous grazing mode (in opposition to the communication mode), which is described in the previous section [16].

Since for the velocities considered the same wavenumbers are the most unstable (see Figure 4 (a)), the base flow is critical to the appearance of the communication mode as it dictates the convective velocity of the dominating instability, with the faster channel (i.e., suction side). However, in the case of lifting conditions or this velocity differential, we see

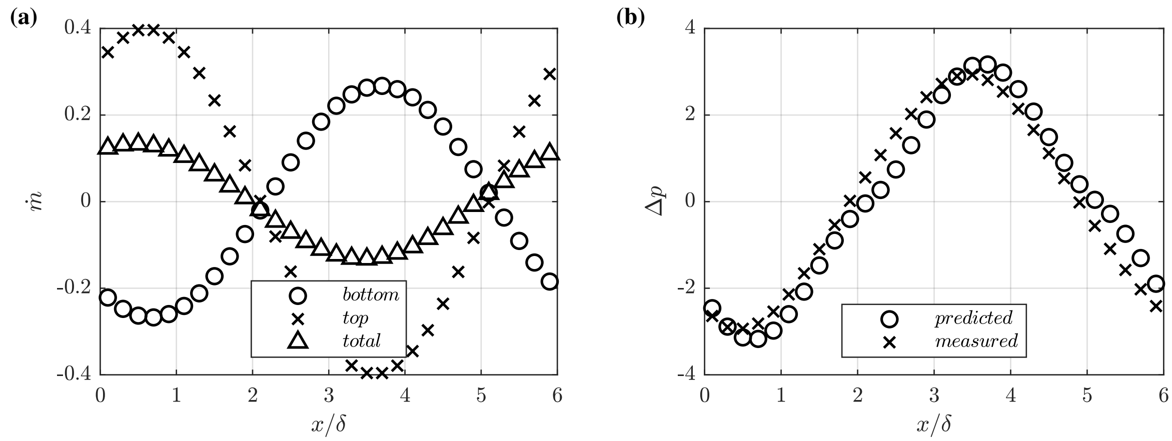

Fig. 14 (a) Mass flow rate and (b) predicted and measured pressure differential across the porous medium at a pressure angle of $\xi = 15°$, $\lambda/\delta = 6$ and $Re_b = 4.5 \times 10^3$.

that the communication mode requires both channels to have the same flow conditions to develop.

We observe in Figure 14 (a) that for the velocity differential case, the net mass flow of the fastest-growing instability across the porous medium is no longer zero due to the emergence of a fluctuating mass flow in the streamwise direction. The symmetry of the perturbation is broken with a velocity differential, and the suction side presents much larger velocity amplitudes (and resulting mass flow) than on the pressure side. This results in a streamwise-varying net mass flow, which would induce additional drag due to the increased flow interaction with the porous medium.

Using the Forchheimer-corrected Darcy law, we can predict the required pressure differential to drive the mass flow through both the bottom and top interfaces, and compare it to the measured pressure differential from the velocity fields. We illustrate this in Figure 14 (b). We find that the velocity differential case leads to a phase lag between the prediction and measurement. This is a result of the required instantaneous pressure differential no longer acting directly normally to the porous medium but at an angle. This further reduces the ability of the communication instability to develop.

Using the definition of communication, both the correlation between the velocities on either side of the porous medium and the mass flow through the medium are greatly reduced. We therefore see that a velocity differential leads to reduced communication, and the shear-like instabilities are more relevant.

C. Linear permeability anisotropy

We investigate the modifications of the system instability due to changes in the linear permeability tensor $\mathbf{K}$ in Figure 15, for a fixed velocity $Re_b = 4.5 \times 10^3$ and wavelength of $\lambda/\delta = 6$. First, we map the growth of the most unstable mode as a function of both the magnitude of the permeability along the principal axes of the tensor by varying its trace $\mathrm{Tr}(\mathbf{K}) \in [1e^{-9},\ 1e^{-7}]$ (corresponding to $Da \in [6 \times 10^{-5}, 6 \times 10^{-3}]$), and the anisotropy of the porous medium by defining a preferential angle $\phi = \mathrm{atan}(\frac{K_{22}}{K_{11}}) \in [5°,\ 85°]$. Second, we compute the growth of the most unstable mode as a function of the diagonal tensor trace $\mathrm{Tr}(\mathbf{K})$ and the diagonal dominance of the permeability tensor defining the

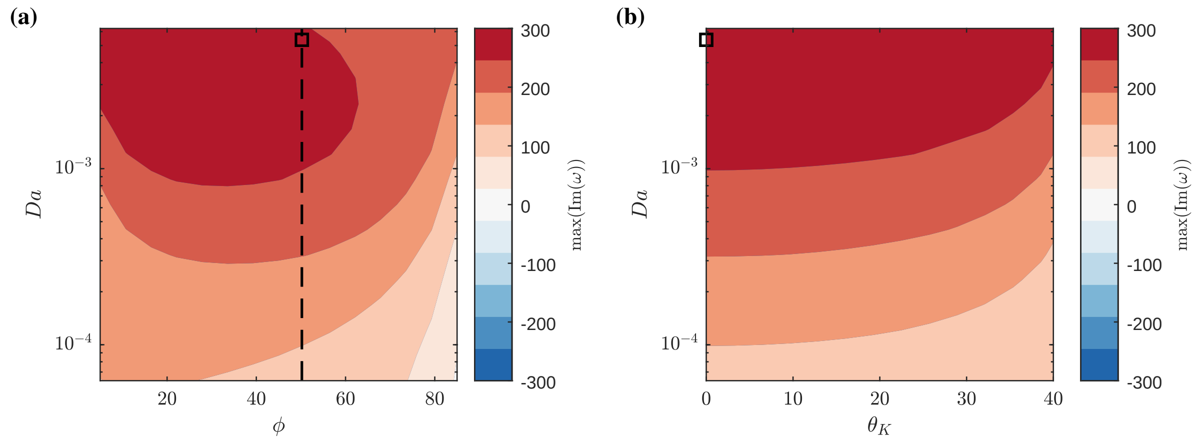

Fig. 15 Growth rate at $\lambda/\delta = 6$ as a function of the Darcy number (a) and the anisotropy angle, and (b) w.r.t. the diagonal preference angle. The dashes and square indicate the reference setup.

angle $\theta = \text{atan}(\frac{2K_{12}}{\text{Tr}(\mathbf{K})}) \in [0°, 45°]$, obtaining the fully populated tensor $\mathbf{K}'$.

We observe in Figure 15 (a) that a wall-normal preferential porous medium (where ϕ is large) is more unstable than a streamwise preferential one. This arises because the base flow is modified by the streamwise permeability, to a greater extent than the non-linear permeability (since it appears in the momentum balance and the velocity in the porous medium is small, so the linear term dominates). The wall-normal preferential medium has a greater velocity gradient at the porous interface, increasing the contribution of the porous terms containing derivatives in Equation 8. Additionally, since the shedding mode is mainly in the wall-normal direction in the porous medium, the permeability in this component facilitates the dominance of this mode. Nonetheless, the streamwise preferential porous medium presents the same instability, albeit at a lower growth rate.

Comparing these results to Rubio Carpio et al. [11], we note that the cited study required greater permeability in an isotropic medium to match the noise reduction of a perforated porous medium (wall-normal preferential). We explain this difference, not by the tortuosity of the medium (since this is not modeled here), but by the anisotropy of the porous medium. For low permeabilities, the system will tend towards the less unstable porous grazing mode, which we can see as the growth rate of the most unstable decreases. In the context of porous trailing edges, the communication can be achieved with a streamwise preferential porous medium, decreasing the likelihood of shedding noise appearing [12].

Further looking at the role of the off-diagonal terms in Figure 15 (b), we note that these terms increase the growth rate of the dominating instability, similarly to the wall-normal permeability increase. However, the instability is mainly dependent on the diagonal terms and the magnitude of the permeability tensor, as the iso-lines indicate.

Having identified the trace of the permeability tensor to be a key parameter, we plot the neutral curve with respect to both this value and the Reynolds number in Figure 16 (a), and the perturbation wavelength in Figure 16 (b). With the first figure, we can conclude that the growth rate of the most unstable mode is mainly a function of the Reynolds number. However, we also observe that increasing the linear permeability of the porous medium increases the growth rate of the

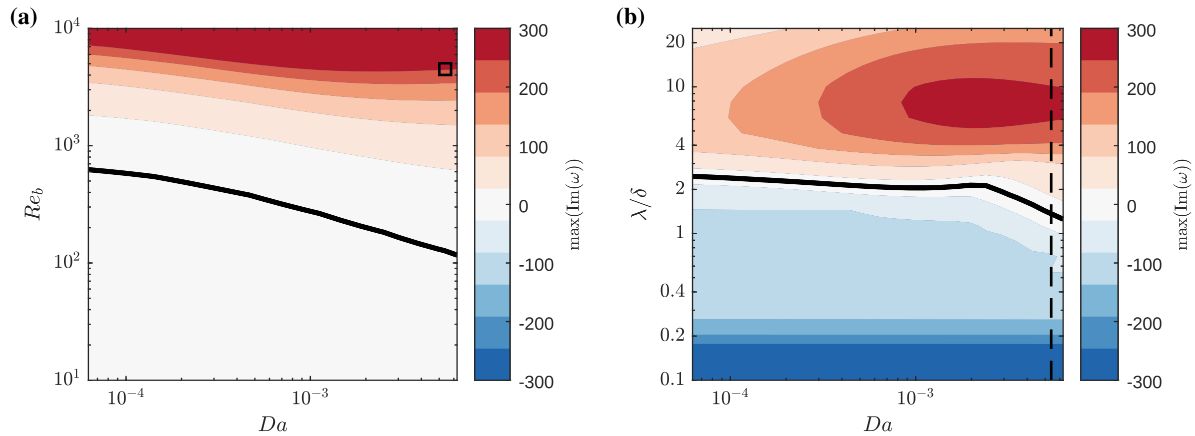

Fig. 16 Growth rate at $\lambda/\delta = 6$ as a function of the Darcy number (a) and bulk Reynolds number, and (b) w.r.t. the wavelength at $Re_b = 4.5 \times 10^3$. Reference setup in dashes and square.

most unstable mode. Similarly, in Figure 16 (b), we find that the wavelength of the most unstable mode is constant for all permeabilities. Thus, the variation of the anisotropy of the linear permeability ϕ is the best approach to modulate the onset of the communication mode. From a design criterion point of view, the analysis points to a more constraining porous extent length $L_{porous} < 4\delta$ to limit the emergence of spanwise coherence as a result of the communication regime.

We show the two instability modes of the small and large permeability in Figure 17. We can observe that the root of the instability shape differs for both cases. In the low permeability case shown in Figure 17 (a), we see in the quiver plot that the velocity magnitude is greater in the channel than in the porous medium. This is the opposite of the communication mode depicted in Figure 17 (b). We further show the different modes by computing the eigenvalue trajectories in Figure 18. In this figure, we note a critical permeability of $Da = 2 \times 10^{-3}$, over which the growth rate of the communication mode ceases to increase, indicating a potential maximum to the amount of communication that can be achieved. An additional criterion can be devised where the Darcy number should not be in excess of 10^{-3} in order to prevent the rapid growth of the instability resulting in the tonal acoustic signature.

D. Non-linear permeability anisotropy

Following the same procedure for the non-linear permeability, we obtain two neutral curves for the alteration of the non-linear permeability shown in Figure 19. In Figure 19 (a), we see that the magnitude of the non-linear permeability has a limited impact on the stability of the system. This differs from purely grazing flows over porous media such as *monami* [20] or flows over porous liners [45]. The latter related the non-linear permeability to inertial effects and viscous phenomena, being a good predictor of drag increase. We find that the non-linear permeability cannot control the onset of the communication through modulating the growth of the communication mode, despite the wall-normal non-linear permeability being documented to play a role in the noise reduction of porous trailing edges [18].

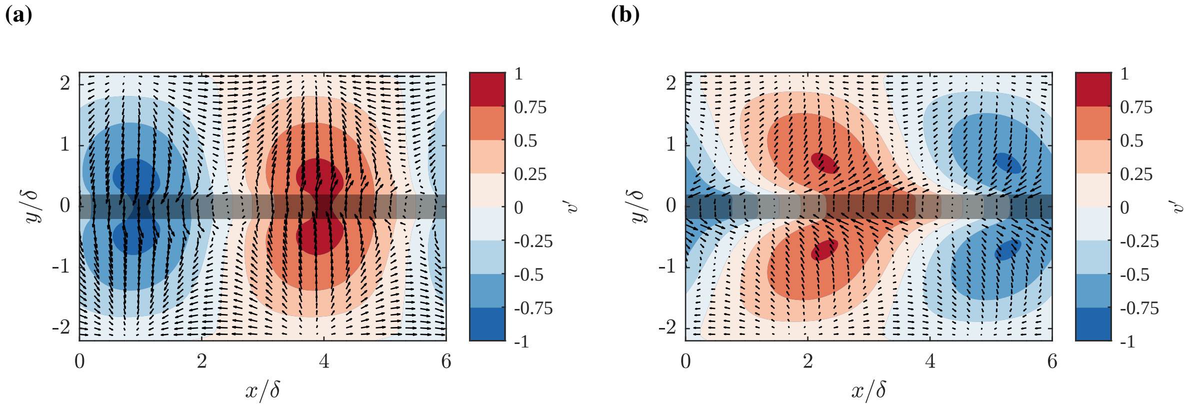

Fig. 17 Contours of the normalised wall-normal velocity, with the arrows indicating the local flow direction, for the most unstable mode shape for (a) $Da = 10^{-4}$ and (b) $Da = 10^{-2}$.

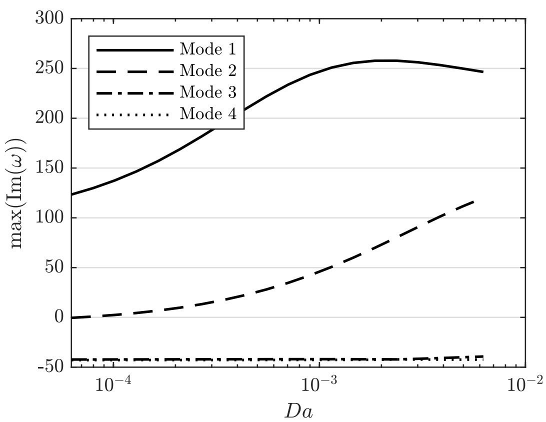

Fig. 18 Growth rate as a function of the Darcy number at $\lambda/\delta = 6$, and $Re_b = 4.5 \times 10^3$ for the four modes with the largest eigenvalue imaginary components.

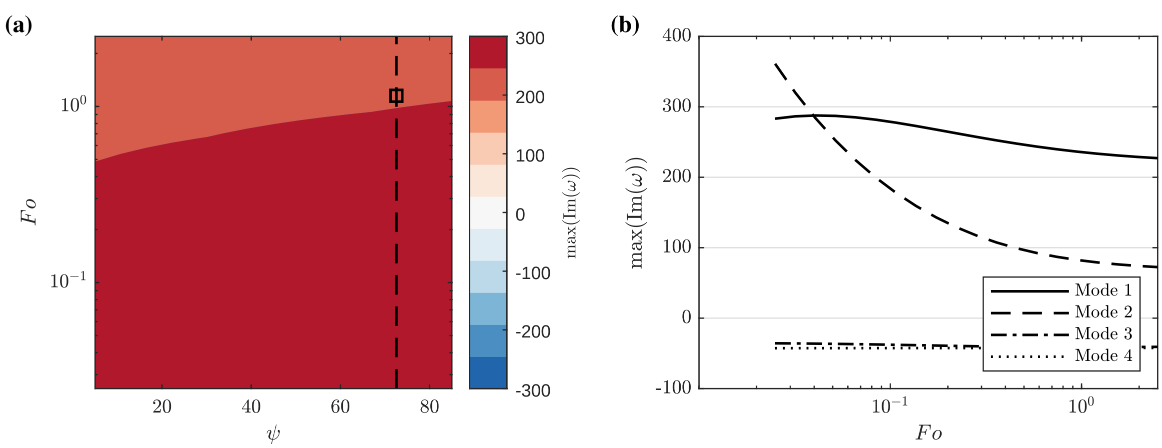

Fig. 19 Growth rate at $\lambda/\delta = 6$ and $Re_b = 4.5 \times 10^3$ as a function of the Forchheimer number (a) and the anisotropy angle, (b) at $\psi = 72°$ (dashes in (a)) for the four fastest-growing perturbations.

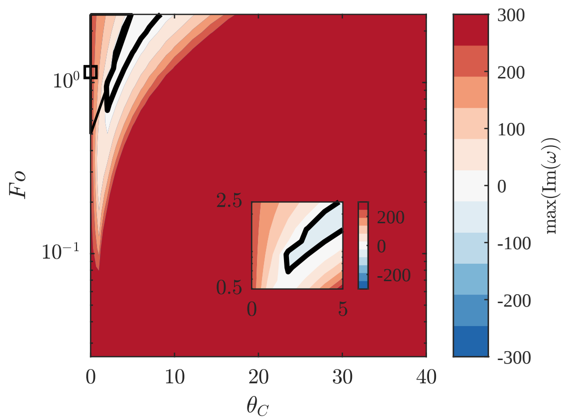

Fig. 20 Growth rate as a function of the Forchheimer number and the diagonal preference angle at $\lambda/\delta = 6$ and $Re_b = 4.5 \times 10^3$. The square indicates the reference parameter.

We show the trajectory of the growth rates of the most unstable modes as a function of the Forchheimer number Fo in Figure 19 (b). We further see that the system is less sensitive to changes of non-linear permeability than to changes in $\mathbf{K}$.

In Figure 20, we find that, unlike the linear permeability, the off-diagonal terms of the non-linear permeability greatly influence the linear stability of the system. We distinguish two regions in the stability map: in the highlighted triangle (also represented in the inset), the communication mode dominates, and outside this triangle, a resonant mode is the most unstable, where the streamwise velocity in the porous medium is the greatest. This secondary mode is a result of the wall-normal velocity being steered away from the y-direction by the off-diagonal term. The interpretability of this instability is therefore judged to fall beyond the scope of the present study, and readers are directed to other work regarding the impact and modeling of the off-diagonal terms on thick porous media [35]. We conclude that the changes in the non-linear permeability have a small impact on the onset of communication.

We therefore confirm a decoupling of the effects of linear and non-linear permeability in the context of communicating wall-bounded flows. The linear permeability acts to modulate the communication, whereas the non-linear permeability acts to modulate the drag increase by controlling the interaction between the porous medium and the wall-bounded flow [15].

E. Ratio of permeabilities

We define the porous Reynolds number $Re_{K/C} = \frac{\mathrm{Tr}(\mathbf{K})/\mathrm{Tr}(\mathbf{C}) \times u_b}{\nu}$ to investigate the relative impact of changes in linear and non-linear permeability. In practice, we choose to keep the non-linear permeability constant to limit the impact of potential spurious instabilities. Sweeping over perturbation wavelength and porous Reynolds number, we obtain Figure 21. In this figure, we see the striking similarity to Figure 16 (b). The main difference is for $Re_{K/C} > 2$, where the system is less linearly unstable across all wavelengths. This indicates that there exists a most unstable point

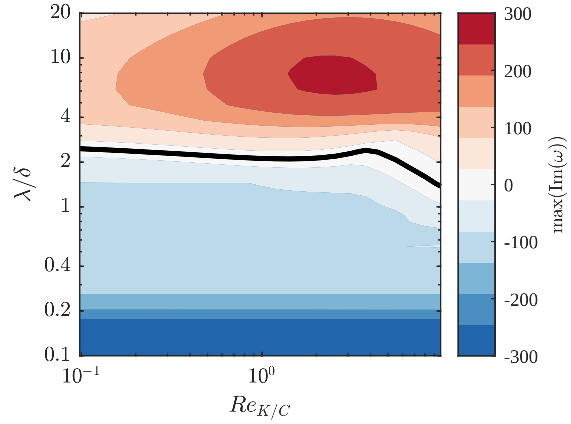

Fig. 21 Growth rate of the most unstable eigenmode as a function of the porous Reynolds number and the perturbation wavelength at $Re_b = 4.5 \times 10^3$.

where the communication mode is most promoted and should be avoided in order to prevent the emergence of spanwise coherent structures. The easiest approach to designing porous trailing edges remains the limit of the porous extent to $L_{porous} < 4\delta$ and where the porous Reynolds number is $Re_{K/C} < 0.5$. The latter criterion ensures that the growth rate of the fastest growing perturbation is halved.

V. Conclusions

In this study, we proposed a novel approach to systematically study the linear stability of communicating wall-bounded flows through a modeled porous medium. This setup is a simplified model for noise-reducing porous trailing edges, and enables the characterisation of the onset of communication in interacting flows through a porous medium. We modeled the porous medium using the Forchheimer-corrected Darcy law. The same dominating instability as the pore-resolved simulation was recovered using the linear stability analysis.

Comparing the results to Poiseuille flow instabilities and grazing flows over porous media, we identified a separate instability that dominated the linear stability of the interacting flows, which we named the communication mode. We characterized the communication mode as the increase in coherence between the channels. It can be quantified using the correlation of the wall-normal velocity between the channels, provided that instantaneous mass flow through the porous medium is achieved. We found this metric to capture well the instantaneous flow through the porous medium.

The relative thickness of the porous medium is a critical parameter to allow for the onset of the communication mode, with the mode dominating from thicknesses $t < 3\delta$ for this specific porous medium. We can use this to formalize the observation that the porous trailing edge should be at most twice as thick as the boundary layer thickness. Moreover, the extent of the porous trailing edge should be limited to the wavelength of the most unstable mode, or about 6δ, and ideally $L_{porous} < 4\delta$ to prevent the emergence of spanwise coherence. Beyond this value, the instantaneous flow through the porous medium would be significant and alter the base flow.

We observed the linear permeability to have a greater impact on the stability of the system than the non-linear permeability. Moreover, we should tailor the permeability anisotropy of the porous medium to delay the onset of the communication mode and the associated shedding noise for large permeability. The off-diagonal terms of the permeability tensors, driving the steering effect, were also shown to have a limited impact on the onset of the communication mode. A porous Reynolds number $Re_{K/C} < 0.5$ would also lead to a halving of the perturbation growth rate.

Finally, we were able to explain the loss of performance of porous trailing edges at lifting conditions by observing that the velocity differential increases the instability of the system by modifying the shape of the primary instability, deviating from the communication mode, and morphing towards the grazing mode. The slower side was entrained by the instability on the faster side. We concluded that the velocity differential led to a breakdown of the communication mode.

We will conduct further work to explore the potential of inhomogeneous porous media, in particular, the wall-normal variation of porous properties, to modulate the decrease in communication with a velocity differential. Limitations arising from the choice of communicating closed channels, and to a limited range of steering angles of the non-linear permeability, justify further exploration of the role and characterisation of steering effects in the communication instability of thin anisotropic porous media. Finally, we plan to explore the spatial development of the communication instability. The convective velocity playing a role in the design criteria of porous trailing edge extent also warrants further investigation of the relationship between growth rate and convective velocity.

Framework verification

We verify the correct implementation of the linear stability framework by computing the linear stability of the first unstable mode of the Poiseuille flow, as documented in [42]. We plot the relative error in both the bulk Reynolds number (dashes) and the first unstable mode (full). The relative error is computed to be the normalised error in a given Quantity of Interest (QoI), Relative error $= QoI_{meas}/QoI_{exact} - 1$, here to be taken as either the bulk Reynolds number or the first unstable eigenvalue. The figure shows that the bulk Reynolds number converges for significantly coarser discretisations than the eigenvalue. This is attributed to the convergence of the evaluation of the derivatives of the base flow that are primordial to the convergence of the eigenvalues. We recover the first unstable eigenvalue at an accuracy of 10^{-4} for $N = 2000$ points, as shown in Figure 22, using the same discretisation as the rest of the manuscript.

We perform the same grid convergence for the C-TCF case [15], as shown in Figure 23. We find that the most unstable communication mode is recovered at an accuracy of 10^{-4} for $N = 2000$ points too. For all the cases considered, we use this resolution, proportionally increasing the number of points for the cases with varying thickness.

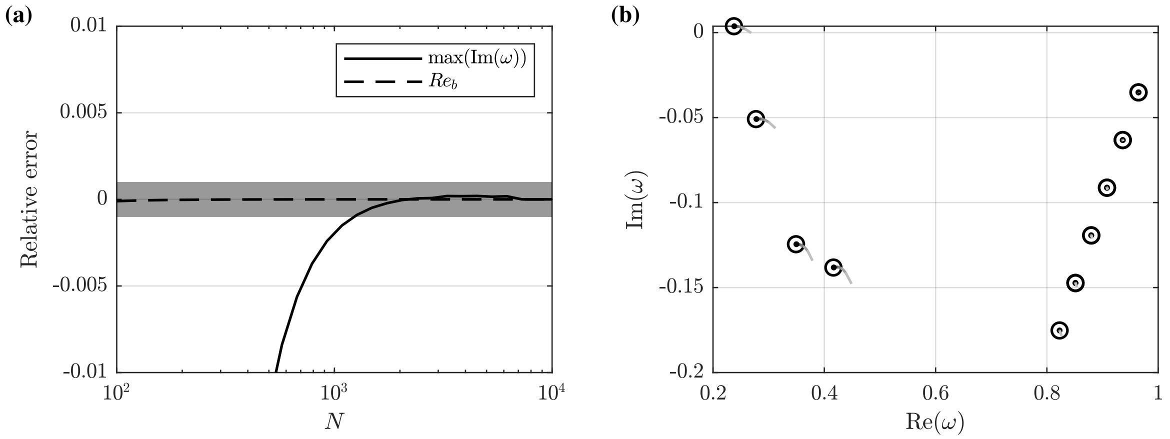

Fig. 22 (a) The relative error in the growth rate and bulk Reynolds number, and (b) the 15 fastest-growing eigenvalues for the Poiseuille flow solution at $Re = 10^4$ and $\alpha = 1$. The lines are coloured as a function of refinement. Dots and circles are the values at $N = 2000$, and from [42].

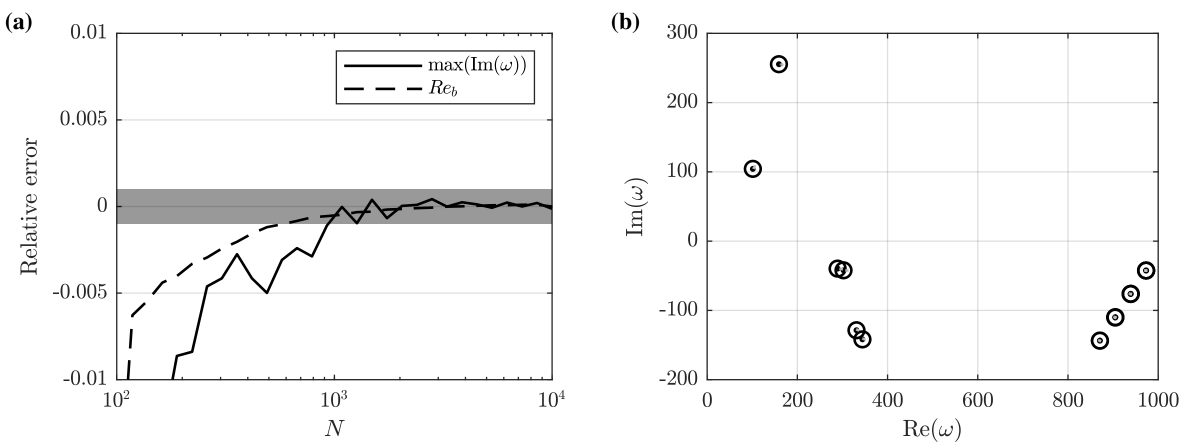

Fig. 23 (a) Relative error in the growth rate and bulk Reynolds number, and (b) the 20 fastest-growing eigenvalues for the C-TCF flow solution at $Re = 2000$ and $\lambda/\delta = 6$. The lines are coloured as a function of refinement. Dots and circles are the values at $N = 2000$, and at the finest refinement.

Funding Sources

This work used the Dutch national e-infrastructure with the support of the SURF Cooperative, using grant no. EINF-8620.

The work of T. P. Hunter is supported by the TU Delft AI Labs & Talent Programme.

The work of F. Avallone is co-funded by the European Union (ERC, LINING, 101075903). Views and opinions expressed are, however, those of the author(s) only and do not necessarily reflect those of the European Union or the European Research Council. Neither the European Union nor the granting authority can be held responsible for them.

All other authors declare that no funding was received for conducting this study, and certify that they have no affiliations with or involvement in any organization or entity with any financial interest or non-financial interest in the subject matter or materials discussed in this manuscript.

References

[1] Jones, L. E., and Sandberg, R. D., "Acoustic and hydrodynamic analysis of the flow around an aerofoil with trailing-edge serrations," *Journal of Fluid Mechanics*, Vol. 706, 2012, pp. 295–322. https://doi.org/10.1017/jfm.2012.254.

[2] Lee, S., Ayton, L. J., Bertagnolio, F., Moreau, S., Chong, T. P., and Joseph, P. F., "Turbulent boundary layer trailing-edge noise: Theory, computation, experiment, and application," *Progress in Aerospace Sciences*, Vol. 126, No. May, 2021, p. 100737. https://doi.org/10.1016/j.paerosci.2021.100737.

[3] Geyer, T., Sarradj, E., and Fritzsche, C., "Porous Airfoils: Noise Reduction and Boundary Layer Effects," *15th AIAA/CEAS Aeroacoustics Conference (30th AIAA Aeroacoustics Conference)*, Vol. 9, American Institute of Aeronautics and Astronautics, Reston, Virigina, 2009, pp. 787–820. https://doi.org/10.2514/6.2009-3392.

[4] Herr, M., Rossignol, K.-S., Delfs, J., Lippitz, N., and Mößner, M., "Specification of Porous Materials for Low-Noise Trailing-Edge Applications," *20th AIAA/CEAS Aeroacoustics Conference*, American Institute of Aeronautics and Astronautics, Reston, Virginia, 2014, pp. 1–19. https://doi.org/10.2514/6.2014-3041.

[5] Teruna, C., Manegar, F. A., Avallone, F., Ragni, D., Casalino, D., and Carolus, T., "Noise reduction mechanisms of an open-cell metal-foam trailing edge," *Journal of Fluid Mechanics*, Vol. 898, 2020. https://doi.org/10.1017/jfm.2020.363.

[6] Ayton, L. J., Colbrook, M. J., Geyer, T. F., Chaitanya, P., and Sarradj, E., "Reducing aerofoil – turbulence interaction noise through chordwise-varying porosity," *Journal of Fluid Mechanics*, Vol. 906, No. A1, 2021. https://doi.org/10.1017/jfm.2020.746.

[7] Breugem, W. P., Boersma, B. J., and Uittenbogaard, R. E., "The influence of wall permeability on turbulent channel flow," *Journal of Fluid Mechanics*, Vol. 562, 2006, p. 35. https://doi.org/10.1017/S0022112006000887.

[8] Shahzad, H., Hickel, S., and Modesti, D., "Permeability and Turbulence Over Perforated Plates," *Flow, Turbulence and Combustion*, Vol. 109, No. 4, 2022, pp. 1241–1254. https://doi.org/10.1007/s10494-022-00337-7.

[9] Kuwata, Y., and Suga, K., "Direct numerical simulation of turbulence over anisotropic porous media," *Journal of Fluid Mechanics*, Vol. 831, 2017, pp. 41–71. https://doi.org/10.1017/jfm.2017.619.

[10] Jiménez, J., Uhlmann, M., Pinelli, A., and Kawahara, G., "Turbulent shear flow over active and passive porous surfaces," *Journal of Fluid Mechanics*, Vol. 442, 2001, pp. 89–117. https://doi.org/10.1017/S0022112001004888.

[11] Rubio Carpio, A., Avallone, F., Ragni, D., Snellen, M., and van der Zwaag, S., "Quantitative criteria to design optimal permeable trailing edges for noise abatement," *Journal of Sound and Vibration*, Vol. 485, 2020, p. 115596. https://doi.org/10.1016/j.jsv.2020.115596.

[12] Luesutthiviboon, S., Ragni, D., Avallone, F., and Snellen, M., "An alternative permeable topology design space for trailing-edge noise attenuation," *International Journal of Aeroacoustics*, Vol. 20, No. 3-4, 2021, pp. 221–253. https://doi.org/10.1177/1475472X211003295.

[13] Geyer, T. F., and Sarradj, E., "Trailing Edge Noise of Partially Porous Airfoils," *20th AIAA/CEAS Aeroacoustics Conference*, American Institute of Aeronautics and Astronautics, Reston, Virginia, 2014, pp. 1–18. https://doi.org/10.2514/6.2014-3039.

[14] Teruna, C., Avallone, F., Ragni, D., and Casalino, D., "On the noise reduction of a porous trailing edge applied to an airfoil at lifting condition," *Physics of Fluids*, Vol. 33, No. 5, 2021, p. 1ENG. https://doi.org/10.1063/5.0047512.

[15] Hunter, T. P., Avallone, F., Doan, N. A. K., and Ragni, D., "Characterization of Communicating Turbulent Grazing Flows Through a Resolved Porous Medium," *Flow, Turbulence and Combustion*, Vol. 116, No. 1, 2026, p. 10. https://doi.org/10.1007/s10494-025-00711-1.

[16] Gómez-de Segura, G., Sharma, A., and García-Mayoral, R., "Turbulent Drag Reduction Using Anisotropic Permeable Substrates," *Flow, Turbulence and Combustion*, Vol. 100, No. 4, 2018, pp. 995–1014. https://doi.org/10.1007/s10494-018-9916-4.

[17] Hunter, T. P., Avallone, F., Doan, N. A. K., and Ragni, D., "Aerodynamic Characterisation of Communicating Turbulent Boundary Layers Through a Porous Medium Subjected to a Pressure Differential," *30th AIAA/CEAS Aeroacoustics Conference (2024)*, American Institute of Aeronautics and Astronautics, Reston, Virginia, 2024. https://doi.org/10.2514/6.2024-3049.

[18] Colbrook, M. J., and Ayton, L. J., "Do we need non-linear corrections? On the boundary Forchheimer equation in acoustic scattering," *Journal of Sound and Vibration*, Vol. 495, 2021, p. 115905. https://doi.org/10.1016/j.jsv.2020.115905.

[19] Abderrahaman-Elena, N., and García-Mayoral, R., "Analysis of anisotropically permeable surfaces for turbulent drag reduction," *Physical Review Fluids*, Vol. 2, No. 11, 2017, p. 114609. https://doi.org/10.1103/PhysRevFluids.2.114609.

[20] Singh, R., Bandi, M. M., Mahadevan, A., and Mandre, S., "Linear stability analysis for monami in a submerged seagrass bed," *Journal of Fluid Mechanics*, Vol. 786, 2015, pp. R1–1–R1–12. https://doi.org/10.1017/jfm.2015.642.

[21] Tilton, N., and Cortelezzi, L., "Linear stability analysis of pressure-driven flows in channels with porous walls," *Journal of Fluid Mechanics*, Vol. 604, 2008, pp. 411–445. https://doi.org/10.1017/S0022112008001341.

[22] Li, Q., Lei, H. Y., and Dai, C. S., "Linear stability of a fluid channel with a porous layer in the center," *Acta Mechanica Sinica/Lixue Xuebao*, Vol. 30, No. 1, 2014, pp. 28–36. https://doi.org/10.1007/s10409-013-0094-2.

[23] Karmakar, S., Usha, R., and Shukla, P., "Linear stability of a plane Poiseuille flow in a three-layered channel with a centered anisotropic porous layer," *International Journal of Heat and Mass Transfer*, Vol. 224, No. February, 2024, p. 125314. https://doi.org/10.1016/j.ijheatmasstransfer.2024.125314.

[24] Chavarin, A., and Luhar, M., "Resolvent analysis for turbulent channel flow with riblets," *AIAA Journal*, Vol. 58, No. 2, 2020, pp. 589–599. https://doi.org/10.2514/1.J058205.

[25] Gómez, F., Blackburn, H. M., Rudman, M., Sharma, A. S., and McKeon, B. J., "Streamwise-varying steady transpiration control in turbulent pipe flow," *Journal of Fluid Mechanics*, Vol. 796, 2016, pp. 588–616. https://doi.org/10.1017/jfm.2016.279.

[26] Chavarin, A., Gómez-De-Segura, G., García-Mayoral, R., and Luhar, M., "Resolvent-based predictions for turbulent flow over anisotropic permeable substrates," *Journal of Fluid Mechanics*, Vol. 913, 2021. https://doi.org/10.1017/jfm.2020.1169.

[27] Jafari, A., McKeon, B. J., Cazzolato, B. C., and Arjomandi, M., "A resolvent analysis of the effect of passive perforated surfaces on wall-bounded turbulence," *International Journal of Heat and Fluid Flow*, Vol. 106, No. December 2023, 2024, pp. 0–10. https://doi.org/10.1016/j.ijheatfluidflow.2024.109315.

[28] Teruna, C., Manegar, F. A., Avallone, F., Casalino, D., Ragni, D., Rubio Carpio, A., and Carolus, T., "Numerical Analysis of Metal-Foam Application for Trailing Edge Noise Reduction," *25th AIAA/CEAS Aeroacoustics Conference*, Vol. 2650, American Institute of Aeronautics and Astronautics, Reston, Virginia, 2019. https://doi.org/10.2514/6.2019-2650.

[29] Hunter, T. P., Doan, N. A. K., Avallone, F., and Ragni, D., "Numerical investigation of communicating turbulent boundary layers through porous media," *INTER-NOISE and NOISE-CON Congress and Conference Proceedings*, Vol. 268, No. 8, 2023, pp. 834–840. https://doi.org/10.3397/IN_2023_0133.

[30] Shahzad, H., Hickel, S., and Modesti, D., "Direct Numerical Simulation of a Turbulent Boundary Layer over Acoustic Liners," *AIAA Journal*, 2025, pp. 1–12. https://doi.org/10.2514/1.j065204.

[31] Vafai, K., and Kim, S. J., "On the limitations of the Brinkman-Forchheimer-extended Darcy equation," *International Journal of Heat and Fluid Flow*, Vol. 16, No. 1, 1995, pp. 11–15. https://doi.org/10.1016/0142-727X(94)00002-T.

[32] Shahzad, H., Hickel, S., and Modesti, D., "Direct Numerical Simulation of a Turbulent Boundary Layer over Acoustic Liners," *AIAA AVIATION 2023 Forum*, American Institute of Aeronautics and Astronautics, Reston, Virginia, 2023, pp. 1–12. https://doi.org/10.2514/6.2023-3887.

[33] Joseph, D. D., Nield, D. A., and Papanicolaou, G., "Nonlinear equation governing flow in a saturated porous medium," *Water Resources Research*, Vol. 18, No. 4, 1982, pp. 1049–1052. https://doi.org/10.1029/WR018i004p01049.

[34] Wang, X., Thauvin, F., and Mohanty, K. K., "Non-Darcy flow through anisotropic porous media," *Chemical Engineering Science*, Vol. 54, No. 12, 1999, pp. 1859–1869. https://doi.org/10.1016/S0009-2509(99)00018-4.

[35] Aghaei-Jouybari, M., Seo, J.-H., Pinto, S., Cattafesta, L., Meneveau, C., and Mittal, R., "Extended Darcy–Forchheimer law including inertial flow deflection effects," *Journal of Fluid Mechanics*, Vol. 980, 2024, p. A13. https://doi.org/10.1017/jfm.2023.1083.

[36] Tsiberkin, K., "Porosity effect on the linear stability of flow overlying a porous medium," *The European Physical Journal E*, Vol. 43, No. 6, 2020, p. 34. https://doi.org/10.1140/epje/i2020-11959-6.

[37] Gómez-De-Segura, G., and García-Mayoral, R., "Turbulent drag reduction by anisotropic permeable substrates-analysis and direct numerical simulations," *Journal of Fluid Mechanics*, Vol. 875, 2019, pp. 124–172. https://doi.org/10.1017/jfm.2019.482.

[38] Sumesh, C. K., and Jothi, T. J. S., "Aerodynamic noise from an asymmetric airfoil with perforated extension plates at the trailing edge," *International Journal of Aeroacoustics*, Vol. 20, No. August 2020, 2021, pp. 88–108. https://doi.org/10.1177/1475472X20978388.

[39] Avallone, F., van der Velden, W. C. P., Ragni, D., and Casalino, D., "Noise reduction mechanisms of sawtooth and combed-sawtooth trailing-edge serrations," *Journal of Fluid Mechanics*, Vol. 848, 2018, pp. 560–591. https://doi.org/10.1017/jfm.2018.377.

[40] Rubio Carpio, A., Avallone, F., and Ragni, D., "On the role of the flow permeability of metal foams on trailing edge noise reduction," *2018 AIAA/CEAS Aeroacoustics Conference*, 2018. https://doi.org/10.2514/6.2018-2964.

[41] Teruna, C., Avallone, F., Ragni, D., Rubio Carpio, A., and Casalino, D., "Numerical analysis of a 3-D printed porous trailing edge for broadband noise reduction," *Journal of Fluid Mechanics*, Vol. 926, 2021, pp. 1–36. https://doi.org/10.1017/jfm.2021.704.

[42] Orszag, S. A., "Accurate solution of the Orr–Sommerfeld stability equation," *Journal of Fluid Mechanics*, Vol. 50, No. 4, 1971, pp. 689–703. https://doi.org/10.1017/S0022112071002842.

[43] Sidiropoulou, M. G., Moutsopoulos, K. N., and Tsihrintzis, V. A., "Determination of Forchheimer equation coefficients a and b," *Hydrological Processes*, Vol. 21, No. 4, 2007, pp. 534–554. https://doi.org/10.1002/hyp.6264, URL http://jamsb.austms.org.au/courses/CSC2408/semester3/resources/ldp/abs-guide.pdfhttps://onlinelibrary.wiley.com/doi/10.1002/hyp.6264.

[44] Ananthan, V. B., Bernicke, P., Akkermans, R. A., Hu, T., and Liu, P., "Effect of porous material on trailing edge sound sources of a lifting airfoil by zonal Overset-LES," *Journal of Sound and Vibration*, Vol. 480, 2020. https://doi.org/10.1016/j.jsv.2020.115386.

[45] Shahzad, H., Hickel, S., and Modesti, D., "Turbulence and added drag over acoustic liners," *Journal of Fluid Mechanics*, Vol. 965, 2023, p. A10. https://doi.org/10.1017/jfm.2023.397.